Effects of Control Loop Interactions on Maximum Power Transfer Capability of Weak-grid-tied Grid-following Inverters

Weihua Zhou, Mohammad Hasan Ravanji, Nabil Mohammed, and Behrooz Bahrani

***Abstract*—The maximum power transfer capability (MPTC) of phase-locked loop (PLL)-based grid-following inverters is often limited under weak-grid conditions due to passivity violations caused by operating-point-dependent control loops. This paper reveals and compares the mechanisms of these violations across different control strategies. Using admittance decomposition and full-order state-space models for eigenvalue analysis, MPTC limitations from control loops and their interactions are identified. The small-signal stabilities of different control loops are compared under varying grid strength, and both static and dynamic MPTCs for each control mode are examined. This paper also explores how control loop interactions impact the MPTC, offering insights for tuning control loops to enhance stability in weak grids. For example, fast power control improves the MPTC when paired with a slow PLL, while power control has minimal effect when the PLL is sufficiently fast. The findings are validated through frequency scanning, eigenvalue analysis, simulations, and experiments.**

***Index Terms*—Grid-following inverter, control loop interaction, power transfer capability, small-signal stability, admittance decomposition, weak grid.**

I. Introduction

PHASE-LOCKED loop (PLL)-based grid-following inverters (GFLIs) are widely used for renewable energy integration [1]. In addition to basic alternating current control (ACC) and PLL, various additional control loops such as active power control (APC), reactive power control (RPC), DC-link voltage control (DVC), and alternating voltage control (AVC) are commonly employed [2], [3]. However, the interactions between these nonlinear control loops and weak grids, characterized by low short-circuit ratios (SCRs), can limit the maximum power transfer capability (MPTC) [4], [5]. Therefore, it is crucial to develop a fundamental understanding of the MPTC limitations imposed by these control loops.

In addition to the dynamic MPTC induced by control interactions, the static MPTC, which depends on grid SCR and reactive power transfer rather than control dynamics, can also be limited by the power-angle relationship [6], [7]. It is assumed in [6] and [7] that the static MPTC is always larger than the dynamic MPTC, and can only be achieved if a sufficiently slow PLL is used. However, whether this assumption consistently holds requires further investigation. In [6], the ACC, APC, and AVC are proven to have negligible effects on the dynamic MPTC compared with the PLL, indicating that the minimum SCR for rated active power injection is 1.32 when only the PLL is considered. In contrast, [8] shows that a faster ACC provides higher positive damping to the point-of-common-coupling (PCC) voltage in the current-control time scale when only the ACC is considered. Nevertheless, focusing solely on the PLL or ACC, as in [6], [8], may oversimplify the dynamic MPTC. The coupling effects of ACC-PLL on dynamic MPTC are explored in [9] - [11], [12] - [14], and [15], [16] to improve the designs of PLL, ACC, and auxiliary stability enhancement modules, respectively. However, the effects of power and voltage control on dynamic MPTC are neglected in [9]-[16].

The effects of APC and DVC on dynamic MPTC are discussed in [17], where both ACC and PLL are omitted, showing that faster DVC and slower APC improve weak-grid stability. In [7] and [18], the effects of APC, AVC, and PLL are examined, while the ACC is still ignored. It is shown in [18] that a fast AVC or PLL enhances dynamic MPTC, while [7] indicates that a slow APC, AVC, or PLL extends dynamic MPTC. In contrast, [19] - [21] consider the effects of APC, AVC, PLL, and ACC, concluding that AVC can reduce dynamic MPTC. However, these studies assume that the cascaded loops are decoupled, thereby overlooking the impact of control interactions on dynamic MPTC.

The control interactions between the DVC and PLL are examined in [22] - [24], showing that instability in the PCC voltage and DC-link voltage can arise from the coupling between the DVC and PLL at high power output. This coupling can be mitigated by increasing the DVC bandwidth or reducing the PLL bandwidth. The control interaction between the DVC and AVC is explored in [25], revealing that

Manuscript received: February 24, 2024; revised: June 3, 2024; accepted: November 7, 2024. Date of CrossCheck: November 7, 2024. Date of online publication: December 4, 2024.

This work was funded by the Australian Renewable Energy Agency (No. 2023/ARP010).

W. Zhou (corresponding author), N. Mohammed, and B. Bahrani are with the Department of Electrical and Computer Systems Engineering, Monash University, Melbourne, 3800 Victoria, Australia (e-mail: weihua. zhou@ieee. org; nabil. mohammed@ieee.org; behrooz.bahrani@monash.edu).

M. H. Ravanji is with the Department of Electrical Engineering, Sharif University of Technology, 14588-89694 Tehran, Iran (e-mail: ravanji@sharif.edu).

DOI: 10.35833/MPCE.2024.000136

the AVC introduces negative damping to the DVC, which can be reduced by increasing the AVC bandwidth. The interaction between APC and PLL is studied in [26]-[29], indicating that a faster APC introduces more negative damping to the PLL-dominant oscillation mode. Further, the control interactions between any two controllers (ACC, PLL, APC, and AVC) are analyzed in [30]. It is shown that a fast ACC and a slow APC improve the dynamic MPTC across a wide range of PLL bandwidth, while a fast AVC increases the MPTC when the PLL bandwidth is low and vice versa. Additionally, APC exhibits minimal coupling with ACC, while increasing the AVC bandwidth clearly improves dynamic MPTC across a wide range of ACC bandwidth. Moreover, reducing the APC bandwidth enhances dynamic MPTC over a wide range of AVC bandwidth.

Based on the above literature review, several research gaps can be identified. First, most existing studies focus on the effects of only one or two control loops such as PLL or ACC, while neglecting the coupling effects between multiple control loops. Second, the state-space and admittance methods employed in prior studies have limitations in capturing insights of eigenvalue analysis and the mechanisms behind passivity violations. Finally, a more systematic and comparative investigation is needed to fully understand the impact of reactive power, considering both static and dynamic MPTCs.

To address the identified research gaps, this paper conducts a comparative analysis of the effects of control loop interactions on both static and dynamic MPTCs, utilizing state-space and admittance methods. The key contributions of this paper are summarized as follows.

1) Sequential derivation of state-space, real-space-vector, and complex-space-vector representations, enabling the analysis of eigenvalue-based dominant-mode relocation and admittance-based passivity violation mechanisms.

2) Decomposed admittance models that reveal the contributions of individual control loops to admittance passivity and identify the coupling effects of the ACC, PLL, and power control on the MPTC.

3) Demonstration that open-loop power control (OLPC) and closed-loop power control (CLPC) have limited effects on admittance reshaping when the PLL is sufficiently fast. However, a fast ACC or power control significantly improves the MPTC when a slow PLL is used.

The remainder of this paper is organized as follows. Section II presents the MPTC of GFLI. The studied system is described, and the impact of the PLL on MPTC is analyzed. Section III explores the effects of OLPC and CLPC on MPTC. Experimental verification is provided in Section IV. Finally, conclusions are drawn in Section V.

II. MPTC OF GFLI

A. System Description

Figure 1 illustrates the single-line diagram of a GFLI, which is equipped with an inductance filter L_{f} and its parasitic resistance R_{f}. The grid impedance is modeled as a resistor R_{g} in series with an inductor L_{g}. A synchronous-reference-frame PLL aligns the phase angle of the injected current with the PCC voltage. The proportional-integral (PI)-controller-based ACC incorporates a PCC-voltage feed-forward channel with coefficient γ, along with dq-axis decoupling capability. Two first-order low-pass filters with time constants T_{v} and T_{i} are used to filter out high-frequency measurement noise from $\boldsymbol{v}_{2,dq}^{\mathrm{c,r}}$ and $\boldsymbol{i}_{\mathrm{g},dq}^{\mathrm{c,r}}$, respectively. The superscript c indicates the controller reference frame, while r denotes the real space vector. Power regulation can be achieved using either OLPC or CLPC. Other parameters are provided in Table SAI in Supplementary Material A.

B. Impact of PLL on MPTC

The theoretical derivation of the admittance interactions between the ACC and PLL is detailed in Supplementary Material B. Building on this, the impact of the PLL on MPTC is investigated as follows.

1) PLL-induced MPTC Ignoring PCC Voltage Variation

The contribution of PLL to the qq- and dq-axis admittance components of $\boldsymbol{Y}_{\mathrm{cl}}^{\mathrm{pll,m}}$ can be derived from (S6) in Supplementary Material B as:

$$\begin{cases} -G_{\mathrm{i,pll},qq}^{\mathrm{m,p}}(s) = \dfrac{-I_{\mathrm{g},d}G_{\mathrm{pll}}}{s+V_{2,d}G_{\mathrm{pll}}} \\ -G_{\mathrm{i,pll},dq}^{\mathrm{m,q}}(s) = \dfrac{I_{\mathrm{g},q}G_{\mathrm{pll}}}{s+V_{2,d}G_{\mathrm{pll}}} \end{cases} \tag{1}$$

where $G_{\mathrm{i,pll},qq}^{\mathrm{m,p}}$ and $G_{\mathrm{i,pll},dq}^{\mathrm{m,q}}$ are the qq-axis component of active-current-related admittance $G_{\mathrm{i,pll}}^{\mathrm{m,p}}$ and the dq-axis component of reactive-current-related admittance $G_{\mathrm{i,pll}}^{\mathrm{m,q}}$, respectively; G_{pll} is the PLL contrller; $I_{\mathrm{g},d}$ and $I_{\mathrm{g},q}$ are the d- and q-axis active currents, respectively; and $V_{2,d}$ is the PCC voltage. At the DC frequency point, (1) becomes:

$$\begin{cases} -G_{\mathrm{i,pll},qq}^{\mathrm{m,p}}(s=0) = \dfrac{-I_{\mathrm{g},d}}{V_{2,d}} \\ -G_{\mathrm{i,pll},dq}^{\mathrm{m,q}}(s=0) = \dfrac{I_{\mathrm{g},q}}{V_{2,d}} \end{cases} \tag{2}$$

Equation (2) indicates that the qq-axis admittance behaves as a negative resistor under inverter mode, while the dq-axis admittance behaves as a negative or positive resistor depending on whether there is reactive current absorption or injection, respectively.

Since the qq-axis admittance component plays a crucial role in determining the MPTC of the GFLI [31], Fig. 2 illustrates the vector diagrams of $-G_{\mathrm{i,pll},qq}^{\mathrm{m,p}}$ expressed in (1), and the qq-axis grid admittance component $Y_{\mathrm{g},qq}^{\mathrm{m}}$, as the active current $I_{\mathrm{g},d}$ and PLL bandwidth ω_{pll} increase. The phase angles of $-G_{\mathrm{i,pll},qq}^{\mathrm{m,p}}$ and $Y_{\mathrm{g},qq}^{\mathrm{m}}$ at the low-frequency point ω_{invest}, denoted as σ and $-\phi$, are confined within $[90°, 180°]$ and $[-90°, 0°]$, respectively. Adverse control interactions are assumed to occur when the phase angle difference exceeds 180° at the point where their magnitudes intersect. It is important to note that accurate stability analysis should be performed using the generalized Nyquist criterion or eigenvalue locus analysis.

Equation (1) shows that excessive d-axis current injection increases the magnitude of $-G_{\mathrm{i,pll},qq}^{\mathrm{m,p}}$ while keeping its phase angle σ unchanged, which induces instability. This behavior is depicted in Fig. 2(a) as:

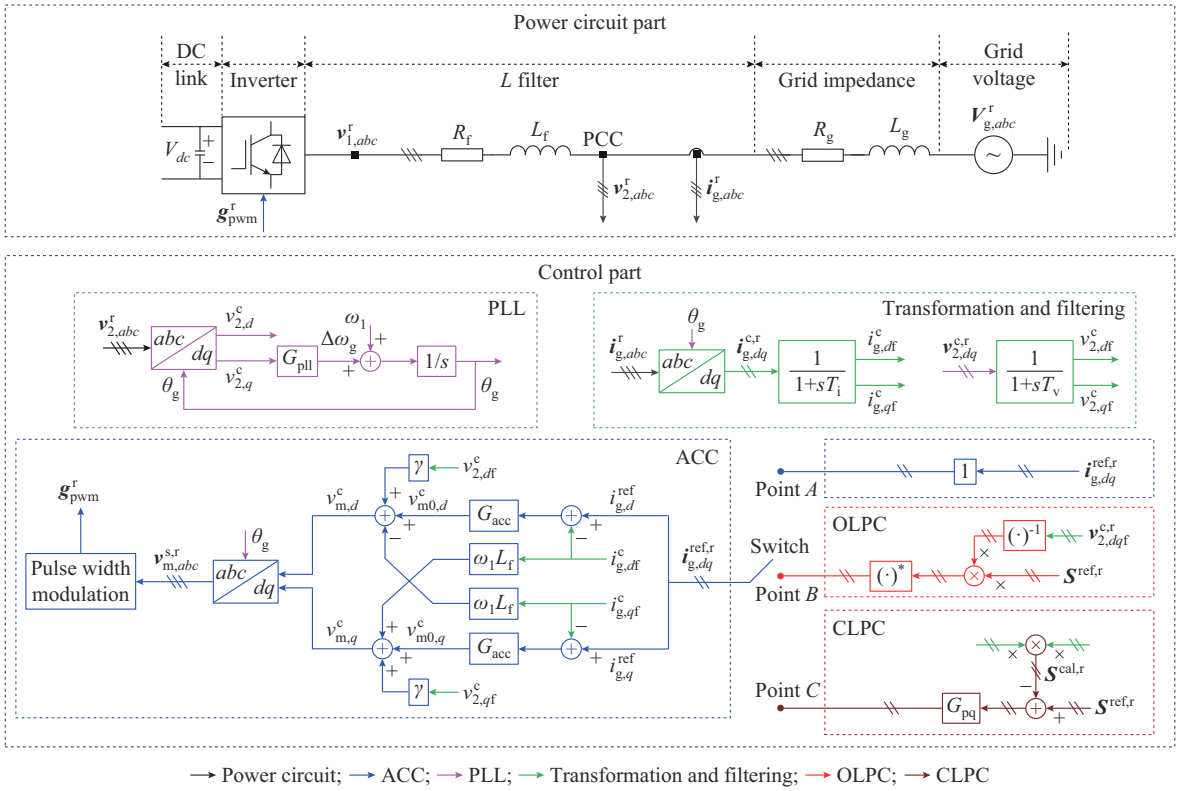

Fig. 1. Single-line diagram of a GFLI.

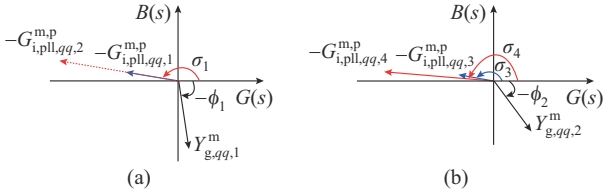

Fig. 2. Vector diagrams of $-G^{\mathrm{m,p}}_{\mathrm{i,pll},qq}$ and $Y^{\mathrm{m}}_{\mathrm{g},qq}$. (a) Increase in active current $I_{\mathrm{g},d}$. (b) Increase in PLL bandwidth ω_{pll}.

$$\begin{cases} \left|-G^{\mathrm{m,p}}_{\mathrm{i,pll},qq,1}\right| < \left|Y^{\mathrm{m}}_{\mathrm{g},qq,1}\right| & \sigma_1+\phi_1>180°, I_{\mathrm{g},d}\ \text{increases} \\ \left|-G^{\mathrm{m,p}}_{\mathrm{i,pll},qq,2}\right| > \left|Y^{\mathrm{m}}_{\mathrm{g},qq,1}\right| & \sigma_1+\phi_1>180°, \text{stability decreases} \end{cases} \tag{3}$$

It can be derived from (1) that a high PLL bandwidth increases both the magnitude and phase angle of $-G^{\mathrm{m,p}}_{\mathrm{i,pll},qq}$, as shown in Supplementary Material C, which induces instability. This behavior is depicted in Fig. 2(b) as:

$$\begin{cases} \left|-G^{\mathrm{m,p}}_{\mathrm{i,pll},qq,3}\right| < \left|Y^{\mathrm{m}}_{\mathrm{g},qq,2}\right| & \sigma_3+\phi_2>180°, \omega_{\mathrm{pll}}\ \text{increases} \\ \left|-G^{\mathrm{m,p}}_{\mathrm{i,pll},qq,4}\right| > \left|Y^{\mathrm{m}}_{\mathrm{g},qq,2}\right| & \sigma_4+\phi_2>180°, \text{stability decreases} \end{cases} \tag{4}$$

The Bode diagrams of the measured and analytical input admittance $\boldsymbol{Y}^{\mathrm{pll,m}}_{\mathrm{cl}}$ of GFLI are plotted, as shown in Fig. 3. In the legend of Fig. 3, the three numbers represent the values of active current $I^{\mathrm{pu}}_{\mathrm{g},d}$, reactive current $I^{\mathrm{pu}}_{\mathrm{g},q}$, and PLL bandwidth ω_{pll}, respectively; and Y_{dd}, Y_{dq}, Y_{qq}, and Y_{qd} are the *dd*-, *dq*-, *qq*-, and *qd*-components of input matrix $\boldsymbol{Y}^{\mathrm{pll,m}}_{\mathrm{cl}}$ of GFLI, respectively. The grid is modeled as an ideal voltage source to maintain the PCC voltage $v^{\mathrm{s}}_{2,d}$ constant. As expected, increased active power injection only increases the *qq*-axis admittance magnitude, while increased reactive power absorption increases only the *dq*-axis admittance magnitude, which is consistent with (1).

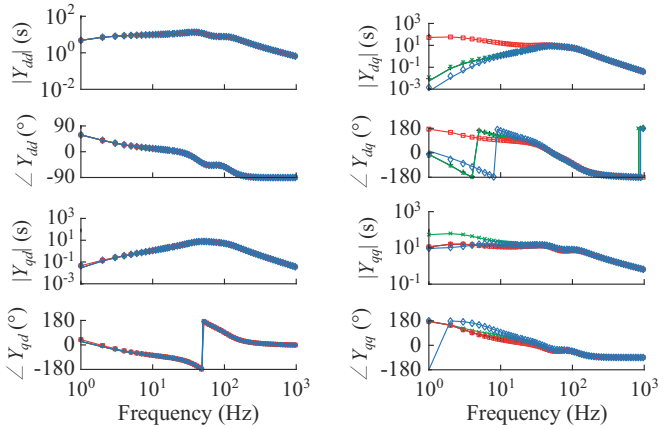

Fig. 3. Effects of active current $I^{\mathrm{pu}}_{\mathrm{g},d}$, reactive current $I^{\mathrm{pu}}_{\mathrm{g},q}$, and PLL bandwidth ω_{pll} on input admittance $\boldsymbol{Y}^{\mathrm{pll,m}}_{\mathrm{cl}}$ of GFLI.

Figure 4 illustrates the eigenvalue loci of the system. The PCC voltage $v^{\mathrm{s}}_{2,d}$ is assumed to remain constant to prevent power-angle-relation violations.

The plot shows that the PLL-induced eigenvalue pair shifts into the right-half plane when high active power is injected. In Fig. 4(a), decreasing the SCR from 3.0 to 2.0 and 1.0 with $\phi=80°$ reduces the PLL-induced dynamic MPTC, denoted as $p^{\mathrm{pu}}_{\mathrm{pll,max}}$, from 2.6 p.u. to 1.1 and 0.1 p.u., respectively. In Fig. 4(b), increasing ω_{pll} from 697 rad/s to 1394 and 2091 rad/s slightly decreases $p^{\mathrm{pu}}_{\mathrm{pll,max}}$ from 1.1 p.u. to 1.0 and 0.9 p.u., respectively. Figure 4(c) shows that increasing q^{pu} from 0.3 p.u. to 0.6 and 0.9 p.u. reduces $p^{\mathrm{pu}}_{\mathrm{pll,max}}$ from 0.9

p.u. to 0.6 and 0.4 p.u., respectively. Lastly, Fig. 4(d) indicates that increasing the ACC bandwidth ω_{acc} from 400 rad/s to 4000 rad/s and 8000 rad/s improves low-frequency stability, aligning with the insights in (S6) of Supplementary Material B. However, higher ω_{acc} results in high-frequency instability induced by time delay. Therefore, a trade-off between high- and low-frequency stability should be considered when tuning the ACC.

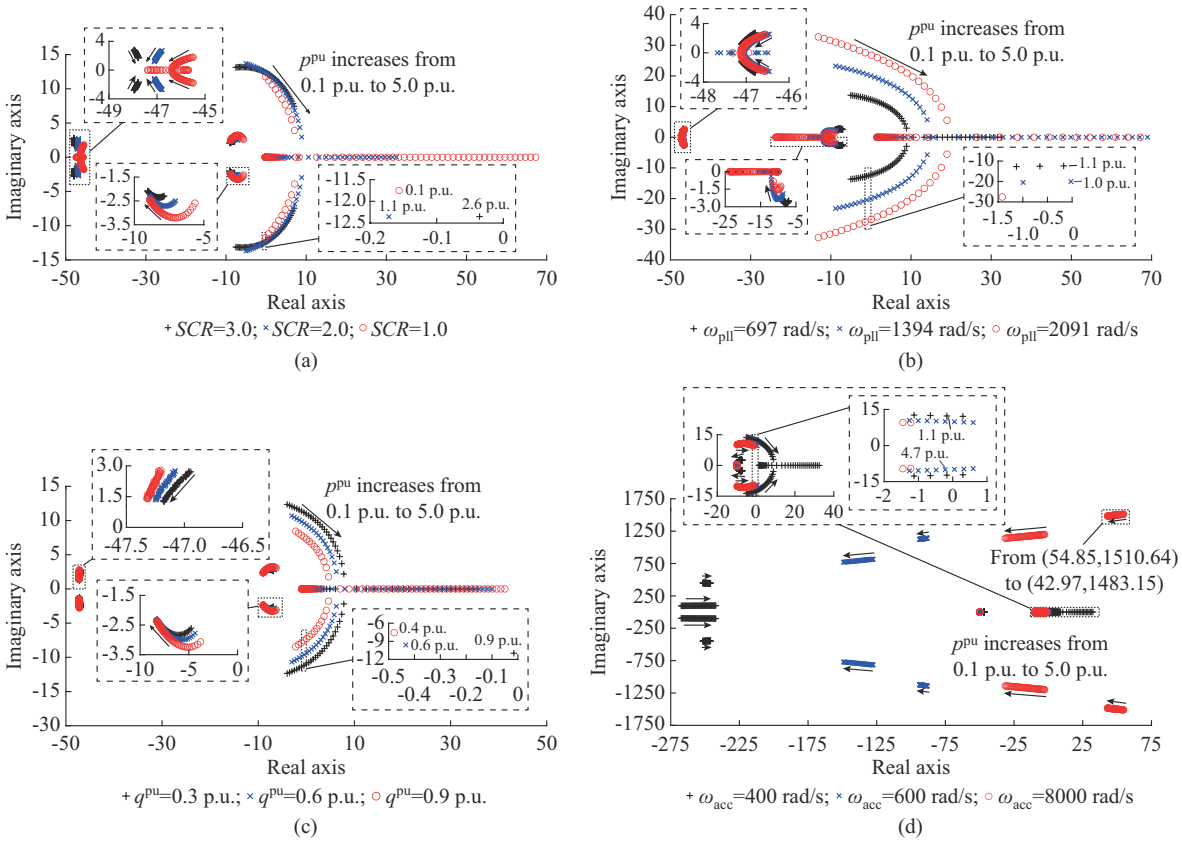

Fig. 4. Eigenvalue loci of system as active power p^{pu} increases from 0.1 p.u. to 5.0 p.u.. (a) SCR changes with $\omega_{pll}=697$ rad/s, $q^{pu}=0$ p.u., and $\omega_{acc}=400$ rad/s. (b) PLL bandwidth ω_{pll} changes with $SCR=2.0$, $q^{pu}=0$ p.u., and $\omega_{acc}=400$ rad/s. (c) Reactive power q^{pu} changes with $SCR=2.0$, $\omega_{pll}=697$ rad/s, and $\omega_{acc}=400$ rad/s. (d) ACC bandwidth ω_{acc} changes with $SCR=2.0$, $\omega_{pll}=697$ rad/s, and $q^{pu}=0$ p.u..

Figure 5(a) shows simulation results of the PLL-induced MPTC $p^{pu}_{pll,max}$ with $SCR=1.0$, $\phi=80°$, and $\omega_{acc}=400$ rad/s. It is evident that when the reference value of reactive power $q^{pu}_{ref}=0$ p.u. and $\omega_{pll}=697$ rad/s, the system becomes unstable and oscillates at 1.8 Hz when the reference value of active power p^{pu}_{ref} increases from 0.1 p.u. to 0.15 p.u. at 25 s, aligning with Fig. 4(a). Stable injection of 0.35 p.u. active power is achieved by decreasing ω_{pll} from 697 rad/s to 69.7 rad/s at 30 s, which corresponds to the behavior of the eigenvalue loci in Fig. 4(b). The system becomes unstable when 0.41 p.u. active power is injected at 45 s and regains stability at 48 s with the injection of 0.5 p.u. reactive power. The power-angle-induced MPTCs without reactive power injection and with 0.5 p.u. reactive power injection p^{pu}_{max1} are 0.4 p.u. and 0.83 p.u., respectively. Thus, the instability observed between 25 s and 30 s and between 45 s and 48 s results from adverse control interaction and violations of power-angle relation, respectively. In Fig. 5(a), p^{pu}_{gfli1} is the maximum transferable active power.

Figure 5(b) presents the simulation results with $SCR=2.0$, $\phi=80°$, $\omega_{pll}=697$ rad/s, $p^{pu}_{ref}=0.1$ p.u., and $q^{pu}_{ref}=0$ p.u.. The system clearly oscillates at 240 Hz when ω_{acc} increases from 4000 rad/s to 8000 rad/s at 1 s, consistent with Fig. 4(d).

2) PLL-induced MPTC Considering PCC Voltage Variation

Since increasing active power injection under an inductive grid slightly decreases the PCC voltage $v^{s}_{2,d}$, this leads to a slight increase in the PLL-related admittance components in (1) and a corresponding decrease in the stability margin. Therefore, the PLL-induced MPTC obtained from Fig. 4(a), (b), and (d) may be marginally higher than the actual PLL-induced MPTC. Specifically, the PLL-induced MPTC with $SCR=1.0$ slightly decreases from 0.119 p.u. in Fig. 4(a) to 0.118 p.u. in Fig. 6(a), confirming this observation.

Since increasing reactive power injection under inductive grid conditions significantly increases $v^{s}_{2,d}$, this results in a noticeable decrease in the PLL-related admittance components in (1) and thus an increase in the stability margin. Consequently, the PLL-induced MPTC observed in Fig. 4(c) may be smaller than the actual PLL-induced MPTC. Specifically, when q^{pu} is 0.3 p.u. and 0.9 p.u., the PLL-induced MPTC increases from 0.90 p.u. and 0.48 p.u. in Fig. 4(c) to 1.00 p.u. and 1.00 p.u. in Fig. 6(b). However, the MPTC decreases when reactive power injection rises to 1.2 p.u. and 1.5 p.u.. Additionally, the oscillation frequency slightly decreases as reactive power injection increases. Figure 6(c) and (d) provides simulation verification of the results shown in Fig. 6(b).

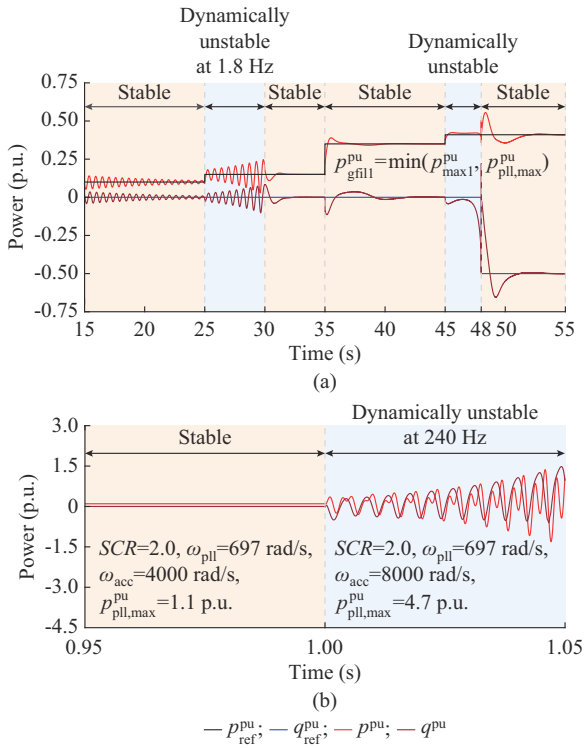

Fig. 5. Time-domain simulation of system. (a) PLL-induced MPTC. (b) ACC-induced high-frequency instability.

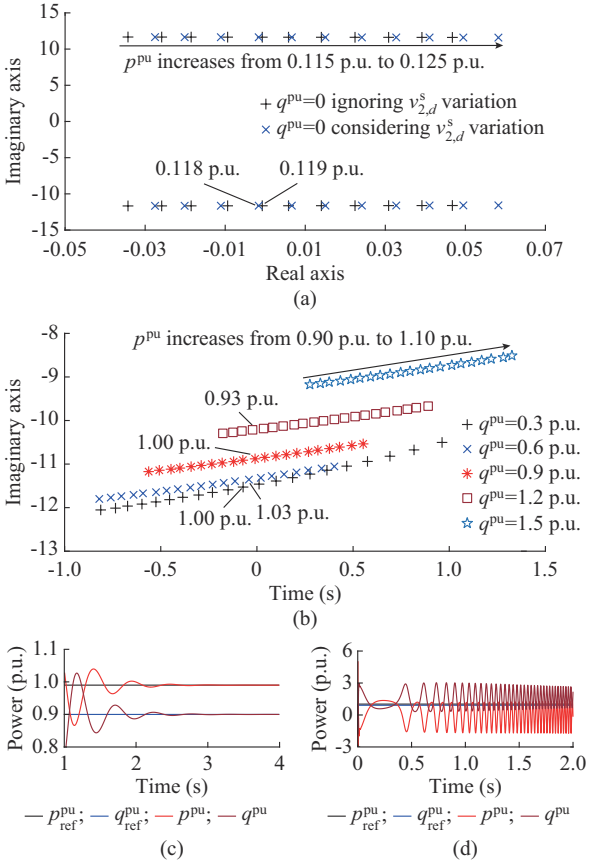

Fig. 6. Eigenvalue loci of system considering variation of PCC voltage $v^{s}_{2,d}$. (a) $SCR=1.0$, $\omega_{pll}=697$ rad/s, $q^{pu}=0$ p.u., and $\omega_{acc}=400$ rad/s. (b) $SCR=2.0$, $\omega_{pll}=697$ rad/s, $q^{pu}=0.3$-1.5 p.u. (with $q^{pu}=0.9$ p.u. as verification), and $\omega_{acc}=400$ rad/s. (c) $p^{pu}_{ref}=0.99$ p.u. and $q^{pu}_{ref}=0.9$ p.u.. (d) $p^{pu}_{ref}=1.01$ p.u., $q^{pu}_{ref}=0.9$ p.u..

Based on Section II, several insights into the MPTC of the ACC-PLL GFLI can be drawn. First, while the ACC itself does not directly limit the MPTC, the PLL-induced MPTC $p^{pu}_{pll,max}$ decreases as the ACC bandwidth ω_{acc} decreases. Second, the power-angle-violation-induced MPTC p^{pu}_{max1} can be considered the theoretical upper limit regardless of the control strategy employed. p^{pu}_{gfli1} decreases from p^{pu}_{max1} to $p^{pu}_{pll,max}$ if the PLL bandwidth ω_{pll} is sufficiently large. Third, increasing the SCR boosts both p^{pu}_{max1} and $p^{pu}_{pll,max}$, while increasing reactive power injection increases p^{pu}_{max1} but decreases $p^{pu}_{pll,max}$.

III. Effects of OLPC and CLPC on MPTC

A. MPTC of GFLI with OLPC

1) Admittance Interactions of ACC, PLL, and OLPC

Based on (S1) in Supplementary Material B and the block diagram of the OLPC in Fig. 7(a), with detailed expressions provided in Supplementary Material D, the closed-loop response of $\Delta\boldsymbol{i}^{s}_{g,dq}$ in Fig. S1(c) considering the OLPC can be derived as:

$$\begin{cases}\Delta\boldsymbol{i}^{s}_{g,dq}=\boldsymbol{G}^{acc}_{cl}\boldsymbol{G}^{ol}_{pq}\Delta\boldsymbol{S}^{ref}+\Delta\boldsymbol{i}^{s1}_{g,dq}+\Delta\boldsymbol{i}^{s2}_{g,dq}+\Delta\boldsymbol{i}^{s3}_{g,dq}\\ \Delta\boldsymbol{i}^{s1}_{g,dq}=\boldsymbol{G}_{i,pll+}\Delta\boldsymbol{v}^{s}_{2,dq}+\boldsymbol{G}_{i,pll-}\Delta\boldsymbol{v}^{s*}_{2,dq}\\ \Delta\boldsymbol{i}^{s2}_{g,dq}=\boldsymbol{Y}^{acc}_{cl}\left(-\boldsymbol{G}_{v,pll+}\Delta\boldsymbol{v}^{s}_{2,dq}-\boldsymbol{G}_{v,pll-}\Delta\boldsymbol{v}^{s*}_{2,dq}\right)\\ \Delta\boldsymbol{i}^{s3}_{g,dq}=\boldsymbol{G}^{acc}_{cl}\boldsymbol{G}^{ol}_{v,pq-}\boldsymbol{G}^{*}_{v,lpf}\left(\boldsymbol{G}^{*}_{v,pll+}\Delta\boldsymbol{v}^{s}_{2,dq}+\boldsymbol{G}^{*}_{v,pll-}\Delta\boldsymbol{v}^{s*}_{2,dq}\right)\end{cases}\tag{5}$$

where $\Delta\boldsymbol{i}^{s1}_{g,dq}$ shows the effect of PLL itself; $\Delta\boldsymbol{i}^{s2}_{g,dq}$ shows the interactions of ACC and PLL; and $\Delta\boldsymbol{i}^{s}_{g,dq}$ shows the interactions of ACC, PLL, and OLPC. The definitions of variables in these equations can be found in Supplementary Material B, and are not given here. Compared with (S5) in Supplementary Material B, the OLPC introduces an additional $\Delta\boldsymbol{i}^{s3}_{g,dq}$ in (5), which can be reformulated as:

$$-\left(\Delta i^{s3}_{g,d}+\mathrm{j}\Delta i^{s3}_{g,q}\right)=\frac{G_{acc}G_{del}(a-\mathrm{j}b)\left(I_{g,d}+\mathrm{j}I_{g,q}\right)}{V_{2,d}(1+sT_{v})(a^{2}+b^{2})}\left(\Delta v^{s}_{2,d}-\mathrm{j}\frac{s\Delta v^{s}_{2,q}}{s+V_{2,d}G_{pll}}\right)\tag{6}$$

$$\begin{cases}a=R_{f}+sL_{f}+G_{acc}G_{del}G_{i,lpf}\\ b=\left(1-G_{del}G_{i,lpf}\right)\omega_{1}L_{f}\end{cases}\tag{7}$$

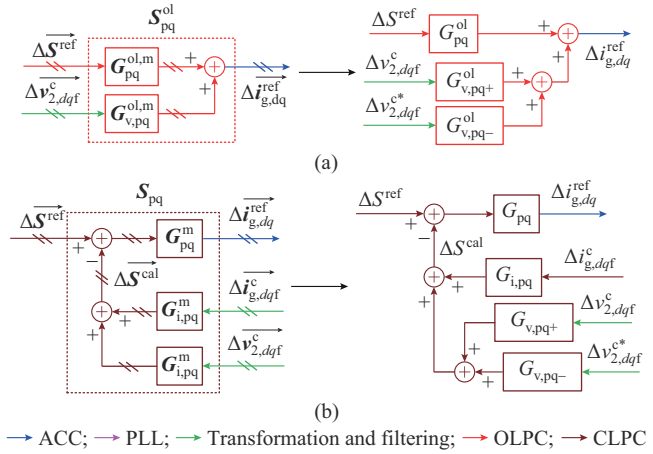

Fig. 7. Reformulation of block diagrams. (a) OLPC. (b) CLPC.

Equation (6) can be reformulated as:

$$-\begin{bmatrix}\Delta i_{\mathrm{g},d}^{\mathrm{s3}}\\ \Delta i_{\mathrm{g},q}^{\mathrm{s3}}\end{bmatrix}=\boldsymbol{Y}_{\mathrm{ol}}^{\mathrm{pc3,m}}\begin{bmatrix}\Delta v_{2,d}^{\mathrm{s}}\\ \Delta v_{2,q}^{\mathrm{s}}\end{bmatrix}=\frac{\boldsymbol{G}_{\mathrm{cl}}^{\mathrm{acc,m}}\boldsymbol{G}_{\mathrm{v,pq}}^{\mathrm{m1}}\boldsymbol{G}_{\mathrm{v,pll}}^{\mathrm{m1}}}{V_{2,d}\left(1+sT_{\mathrm{v}}\right)}\begin{bmatrix}\Delta v_{2,d}^{\mathrm{s}}\\ \Delta v_{2,q}^{\mathrm{s}}\end{bmatrix}\tag{8}$$

$$\begin{cases}\boldsymbol{G}_{\mathrm{cl}}^{\mathrm{acc,m}}=\dfrac{G_{\mathrm{acc}}G_{\mathrm{del}}}{a^2+b^2}\begin{bmatrix}a & b\\ -b & a\end{bmatrix}\\ \boldsymbol{G}_{\mathrm{v,pll}}^{\mathrm{m1}}=\begin{bmatrix}1 & 0\\ 0 & \dfrac{-s}{s+V_{2,d}G_{\mathrm{pll}}}\end{bmatrix}\\ \boldsymbol{G}_{\mathrm{v,pq}}^{\mathrm{m1}}=\begin{bmatrix}I_{\mathrm{g},d} & -I_{\mathrm{g},q}\\ I_{\mathrm{g},q} & I_{\mathrm{g},d}\end{bmatrix}\end{cases}\tag{9}$$

The definitions of variables in the above equations can be found in Supplementary Material B. Clearly, $\boldsymbol{G}_{\mathrm{v,pll}}^{\mathrm{m1}}$ makes the contribution of OLPC to the input admittance asymmetry. Furthermore, $\boldsymbol{Y}_{\mathrm{ol}}^{\mathrm{pc3,m}}$ in (8) can be decomposed as:

$$\boldsymbol{Y}_{\mathrm{ol}}^{\mathrm{pc3,m}}=\boldsymbol{Y}_{\mathrm{ol}}^{\mathrm{pc3,m,p}}+\boldsymbol{Y}_{\mathrm{ol}}^{\mathrm{pc3,m,q}}=\frac{G_{\mathrm{acc}}G_{\mathrm{del}}\begin{bmatrix}a & \dfrac{-bs}{s+V_{2,d}G_{\mathrm{pll}}}\\ -b & \dfrac{-as}{s+V_{2,d}G_{\mathrm{pll}}}\end{bmatrix}I_{\mathrm{g},d}}{V_{2,d}\left(1+sT_{\mathrm{v}}\right)\left(a^2+b^2\right)}+\frac{G_{\mathrm{acc}}G_{\mathrm{del}}\begin{bmatrix}b & \dfrac{as}{s+V_{2,d}G_{\mathrm{pll}}}\\ a & \dfrac{-bs}{s+V_{2,d}G_{\mathrm{pll}}}\end{bmatrix}I_{\mathrm{g},q}}{V_{2,d}\left(1+sT_{\mathrm{v}}\right)\left(a^2+b^2\right)}\tag{10}$$

where $\boldsymbol{Y}_{\mathrm{ol}}^{\mathrm{pc3,m,p}}$ and $\boldsymbol{Y}_{\mathrm{ol}}^{\mathrm{pc3,m,q}}$ represent the admittance components of $\boldsymbol{Y}_{\mathrm{ol}}^{\mathrm{pc3,m}}$ related to active current and reactive current, respectively. Similar to the effect of the PLL on the input admittance of the GFLI $\boldsymbol{Y}_{\mathrm{cl}}^{\mathrm{pll,m}}$, the PLL does not influence the *dd*- and *qd*-axis components of $\boldsymbol{Y}_{\mathrm{ol}}^{\mathrm{pc3,m}}$. However, the ACC, PLL, and OLPC all impact the *dq*- and *qq*-axis admittance components. Unlike the effects of active and reactive currents on $\boldsymbol{Y}_{\mathrm{cl}}^{\mathrm{pll,m}}$, both the active and reactive currents influence all four admittance components of $\boldsymbol{Y}_{\mathrm{ol}}^{\mathrm{pc3,m}}$. Since $a>b$, the active current predominantly affects the *dd*- and *qq*-axis admittance components, while the reactive current primarily influences the *dq*- and *qd*-axis components. Figure 8(a), derived from (5), presents the equivalent circuit model of the GFLI with OLPC. In this model, the impedance/admittance contributions from the filter, ACC, active current via PLL, reactive current via PLL, active current via OLPC, and reactive current via OLPC are represented by $\boldsymbol{Z}_1^{\mathrm{m}}$, $\boldsymbol{Z}_2^{\mathrm{m}}$, $\boldsymbol{Y}_3^{\mathrm{m}}$, $\boldsymbol{Y}_4^{\mathrm{m}}$, $\boldsymbol{Y}_5^{\mathrm{m}}$, and $\boldsymbol{Y}_6^{\mathrm{m}}$, respectively. The corresponding expressions are provided in the fourth row of Table I, where $\boldsymbol{Z}_1^{\mathrm{m}}$, $\boldsymbol{Z}_2^{\mathrm{m}}$, $\boldsymbol{Y}_3^{\mathrm{m}}$-$\boldsymbol{Y}_8^{\mathrm{m}}$ represent the impedance/admittance components induced by the *L* filter, ACC, active current effect via PLL, reactive current effect via PLL, active current effect via OLPC, reactive current effect via OLPC, active current effect via CLPC, and reactive current effect via CLPC, respectively.

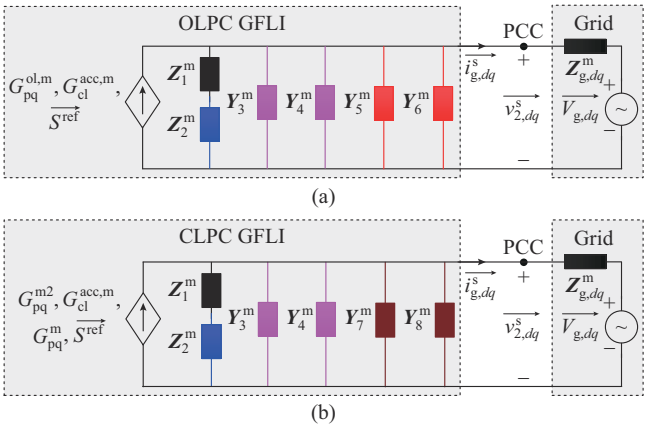

Fig. 8. Equivalent circuit model of system. (a) GFLI with OLPC. (b) GFLI with CLPC.

TABLE I
EXPRESSIONS OF DECOMPOSED IMPEDANCE/ADMITTANCE COMPONENTS

Control	$\boldsymbol{Z}_1^{\mathrm{m}}$	$\boldsymbol{Z}_2^{\mathrm{m}}$	$\boldsymbol{Y}_3^{\mathrm{m}}$	$\boldsymbol{Y}_4^{\mathrm{m}}$	$\boldsymbol{Y}_5^{\mathrm{m}}$	$\boldsymbol{Y}_6^{\mathrm{m}}$	$\boldsymbol{Y}_7^{\mathrm{m}}$	$\boldsymbol{Y}_8^{\mathrm{m}}$
GFLI with ACC	$\boldsymbol{Z}_{\mathrm{cl}}^{\mathrm{acc1,m}}$	$\boldsymbol{Z}_{\mathrm{cl}}^{\mathrm{acc2,m}}$						
GFLI with ACC-PLL	$\left(\boldsymbol{G}_{\mathrm{v,pll}}^{\mathrm{m}}\right)^{-1}\boldsymbol{Z}_{\mathrm{cl}}^{\mathrm{acc1,m}}$	$\left(\boldsymbol{G}_{\mathrm{v,pll}}^{\mathrm{m}}\right)^{-1}\boldsymbol{Z}_{\mathrm{cl}}^{\mathrm{acc2,m}}$	$-\boldsymbol{G}_{\mathrm{i,pll}}^{\mathrm{m,p}}$	$-\boldsymbol{G}_{\mathrm{i,pll}}^{\mathrm{m,q}}$				
GFLI with OLPC	$\left(\boldsymbol{G}_{\mathrm{v,pll}}^{\mathrm{m}}\right)^{-1}\boldsymbol{Z}_{\mathrm{cl}}^{\mathrm{acc1,m}}$	$\left(\boldsymbol{G}_{\mathrm{v,pll}}^{\mathrm{m}}\right)^{-1}\boldsymbol{Z}_{\mathrm{cl}}^{\mathrm{acc2,m}}$	$-\boldsymbol{G}_{\mathrm{i,pll}}^{\mathrm{m,p}}$	$-\boldsymbol{G}_{\mathrm{i,pll}}^{\mathrm{m,q}}$	$\boldsymbol{Y}_{\mathrm{ol}}^{\mathrm{pc3,m,p}}$	$\boldsymbol{Y}_{\mathrm{ol}}^{\mathrm{pc3,m,q}}$		
GFLI with CLPC	$\boldsymbol{G}_{\mathrm{pq}}^{\mathrm{m2}}\left(\boldsymbol{G}_{\mathrm{v,pll}}^{\mathrm{m}}\right)^{-1}\boldsymbol{Z}_{\mathrm{cl}}^{\mathrm{acc1,m}}$	$\boldsymbol{G}_{\mathrm{pq}}^{\mathrm{m2}}\left(\boldsymbol{G}_{\mathrm{v,pll}}^{\mathrm{m}}\right)^{-1}\boldsymbol{Z}_{\mathrm{cl}}^{\mathrm{acc2,m}}$	$-\boldsymbol{G}_{\mathrm{i,pll}}^{\mathrm{m,p}}$	$-\boldsymbol{G}_{\mathrm{i,pll}}^{\mathrm{m,q}}$			$\boldsymbol{Y}_{\mathrm{cl}}^{\mathrm{pc5,m,p}}$	$\boldsymbol{Y}_{\mathrm{cl}}^{\mathrm{pc5,m,q}}$

2) OLPC-induced MPTC

Figure 9 illustrates the vector diagrams of the *qq*-axis components of $\boldsymbol{Y}_{\mathrm{ol}}^{\mathrm{pc3,m,p}}$ and $\boldsymbol{Y}_{\mathrm{ol}}^{\mathrm{pc3,m,q}}$ in (10), i.e., $Y_{\mathrm{ol},qq}^{\mathrm{pc3,m,p}}$ and $Y_{\mathrm{ol},qq}^{\mathrm{pc3,m,q}}$, at the investigated low-frequency point ω_{invest}. Figure 9(a) shows that increasing active current injection increases the admittance magnitude while keeping its phase angle σ_1 between $(90°, 180°)$ unchanged. Similarly, increasing the reactive current absorption increases the admittance magnitude and maintains its phase angle σ_2 between $(-90°, 0°)$ unchanged. This implies that active current injection weakens system stability, while reactive current absorption improves it. Additionally, the OLPC directly links reactive current to the *qq*-axis admittance, which contrasts with the case of GFLI with ACC-PLL, where the *qq*-axis admittance is indirectly influenced by the reactive current through PCC voltage perturbation. In addition, Fig. 9 (b) shows that increasing the PLL bandwidth ω_{pll} decreases the magnitudes of $Y_{\mathrm{ol},qq}^{\mathrm{pc3,m,p}}$ and $Y_{\mathrm{ol},qq}^{\mathrm{pc3,m,q}}$. This suggests that the *dq*- and *qq*-axis admittance components of GFLI with ACC-PLL and OLPC may become similar if the PLL bandwidth is sufficiently wide.

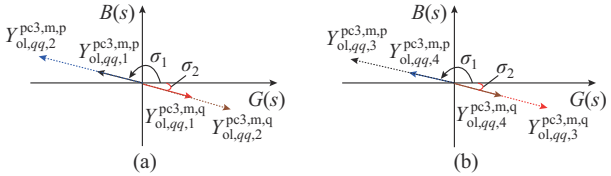

Fig. 9. Vector diagrams of $Y_{\mathrm{ol},qq}^{\mathrm{pc3,m,p}}$ and $Y_{\mathrm{ol},qq}^{\mathrm{pc3,m,q}}$. (a) Variations in active and reactive currents. (b) Changes in PLL bandwidth ω_{pll}.

Figure 10 shows the measured and analytical input admittances of the GFLI with OLPC, where in the legend, the three numbers represent the values of active current $I_{g,d}^{pu}$, reactive current $I_{g,q}^{pu}$, and PLL bandwidth ω_{pll}, respectively. The grid is emulated as an ideal voltage source to maintain a constant PCC voltage $v_{2,d}^{s}$. Clearly, increased active or reactive power injection raises the magnitudes of all four admittance components, which is consistent with (10).

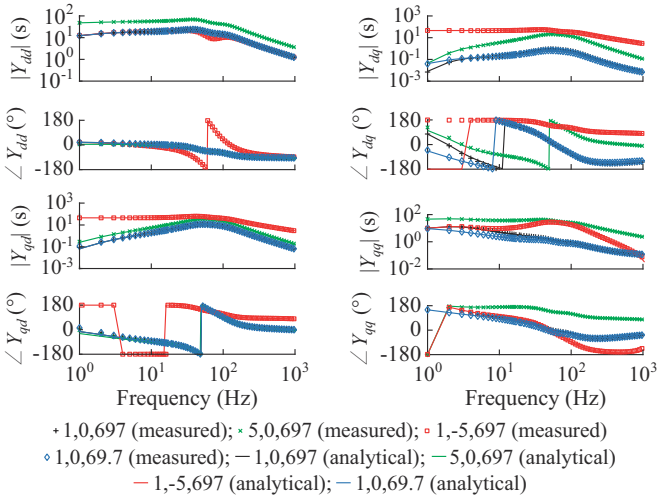

Fig. 10. Measured and analytical input admittances of GFLI with OLPC.

Additionally, the PLL influences only the *dq*- and *qq*-axis admittance components, which also aligns with (10). The DC admittance of the GFLI with OLPC in Fig. 10 is $-\boldsymbol{G}_{v,pq}^{ol,m}$, which agrees with Fig. 7(a). Specifically, the DC *dd*-, *dq*-, *qd*-, and *qq*-axis admittance components behave as positive, negative, negative, and negative resistors, respectively, when active current is injected and reactive current is absorbed.

Figure 11 illustrates the eigenvalue loci of the system with OLPC as the active power p^{pu} increases, assuming a constant PCC voltage $v_{2,d}^{s}$ to avoid violation of power-angle relation. In Fig. 11(a), reducing the SCR from 3.0 to 2.0 and 1.0 with $\phi=80°$ decreases the OLPC-induced MPTC $p_{olpc,max}^{pu}$ from 1.4 p.u. to 0.8 p.u. and 0.1 p.u., respectively. Figure 11(b) shows that increasing ω_{pll} from 697 rad/s to 1394 rad/s and 2091 rad/s leaves $p_{olpc,max}^{pu}$ almost unchanged at 0.8 p.u.. Compared with Fig. 4(b), an additional eigenvalue induced by the OLPC appears at the origin. In Fig. 11(c), increasing q^{pu} from 0.3 p.u. to 0.6 p.u. and 0.9 p.u. slightly reduces $p_{olpc,max}^{pu}$ from 0.7 p.u. to 0.6 p.u. and 0.4 p.u.. Finally, Fig. 11(d) demonstrates that increasing the ACC bandwidth ω_{acc} from 400 rad/s to 600 rad/s and 800 rad/s improves the low-frequency stability.

Figure 12(a) shows the eigenvalue loci of the system considering variations in PCC voltage $v_{2,d}^{s}$. The figure demonstrates that the MPTC $p_{olpc,max}^{pu}$ increases as q^{pu} increases from 0.3 p.u. to 0.9 p.u., but decreases when q^{pu} further increases from 0.9 p.u. to 1.5 p.u.. Unlike the oscillation frequency of GFLI with ACC-PLL shown in Fig. 6(b), the oscillation frequency of the GFLI with OLPC slightly increases as q^{pu} increases. Figure 13 shows the Bode diagrams of the *dq*- and *qq*-axis admittance components of the GFLIs with ACC-PLL, OLPC, and CLPC as the PLL bandwidth ω_{pll} increases. This indicates that when the PLL is sufficiently fast, the PLL and OLPC contribute independently to the input admittance, with no coupling between them, which aligns with the insight derived from (12).

B. MPTC of GFLI with CLPC

1) Admittance Interactions of ACC, PLL, and CLPC

The closed-loop response of $\Delta\boldsymbol{i}_{g,dq}^{s}$ in Fig. SB1(c) in Supplementary Material B considering the CLPC can be derived as (11), where the definitions of variables can be found in the Supplementary Material B.

$$\begin{cases}\Delta\boldsymbol{i}_{g,dq}^{s}=\dfrac{\boldsymbol{G}_{cl}^{acc}\boldsymbol{G}_{pq}\Delta\boldsymbol{S}^{ref}}{1+\boldsymbol{G}_{cl}^{acc}\boldsymbol{G}_{pq}\boldsymbol{G}_{i,pq}\boldsymbol{G}_{i,lpf}}+\Delta\boldsymbol{i}_{g,dq}^{s1}+\Delta\boldsymbol{i}_{g,dq}^{s4}+\Delta\boldsymbol{i}_{g,dq}^{s5}\\ \Delta\boldsymbol{i}_{g,dq}^{s1}=\boldsymbol{G}_{i,pll+}\Delta\boldsymbol{v}_{2,dq}^{s}+\boldsymbol{G}_{i,pll-}\Delta\boldsymbol{v}_{2,dq}^{s*}\\ \Delta\boldsymbol{i}_{g,dq}^{s4}=\dfrac{\boldsymbol{Y}_{cl}^{acc}\left(-\boldsymbol{G}_{v,pll+}\Delta\boldsymbol{v}_{2,dq}^{s}-\boldsymbol{G}_{v,pll-}\Delta\boldsymbol{v}_{2,dq}^{s*}\right)}{1+\boldsymbol{G}_{cl}^{acc}\boldsymbol{G}_{pq}\boldsymbol{G}_{i,pq}\boldsymbol{G}_{i,lpf}}\\ \Delta\boldsymbol{i}_{g,dq}^{s5}=\dfrac{\boldsymbol{G}_{cl}^{acc}\boldsymbol{G}_{pq}\boldsymbol{G}_{v,pq-}\boldsymbol{G}_{v,lpf}^{*}\left(-\boldsymbol{G}_{v,pll-}^{*}\Delta\boldsymbol{v}_{2,dq}^{s}-\boldsymbol{G}_{v,pll+}^{*}\Delta\boldsymbol{v}_{2,dq}^{s*}\right)}{1+\boldsymbol{G}_{cl}^{acc}\boldsymbol{G}_{pq}\boldsymbol{G}_{i,pq}\boldsymbol{G}_{i,lpf}}\end{cases}\tag{11}$$

$\Delta\boldsymbol{i}_{g,dq}^{s5}$ can be reformulated as:

$$-\left(\Delta i_{g,d}^{s5}+\mathrm{j}\Delta i_{g,q}^{s5}\right)=\frac{1}{c}\boldsymbol{G}_{pq}\left(d-\mathrm{j}b\right)\left(I_{g,d}+\mathrm{j}I_{g,q}\right)\cdot\left(\Delta v_{2,d}^{s}-\mathrm{j}\frac{s}{s+V_{2,d}G_{pll}}\Delta v_{2,q}^{s}\right)\tag{12}$$

$$\begin{cases}c=\dfrac{1}{G_{acc}G_{del}}\left(1+sT_{v,lpf}\right)\left(d^2+b^2\right)\\ d=a+V_{2,d}G_{i,lpf}G_{acc}G_{del}G_{pq}\end{cases}\tag{13}$$

Equation (12) can be reformulated as:

$$-\begin{bmatrix}\Delta i_{g,d}^{s5}\\ \Delta i_{g,q}^{s5}\end{bmatrix}=\boldsymbol{Y}_{cl}^{pc5,m}\begin{bmatrix}\Delta v_{2,d}^{s}\\ \Delta v_{2,q}^{s}\end{bmatrix}=\boldsymbol{G}_{pq}^{m1}\boldsymbol{G}_{v,pq}^{m1}\boldsymbol{G}_{v,pll}^{m1}\begin{bmatrix}\Delta v_{2,d}^{s}\\ \Delta v_{2,q}^{s}\end{bmatrix}\tag{14}$$

where $\boldsymbol{G}_{pq}^{m1}=\dfrac{\boldsymbol{G}_{pq}}{c}\begin{bmatrix}d & b\\ -b & d\end{bmatrix}$. Equation (14) can be further decomposed as:

$$\boldsymbol{Y}_{cl}^{pc5,m}=\boldsymbol{Y}_{cl}^{pc5,m,p}+\boldsymbol{Y}_{cl}^{pc5,m,q}=\begin{bmatrix}d & \dfrac{-bs}{s+V_{2,d}G_{pll}}\\ -b & \dfrac{-ds}{s+V_{2,d}G_{pll}}\end{bmatrix}\frac{\boldsymbol{G}_{pq}I_{g,d}}{c}+\begin{bmatrix}b & \dfrac{ds}{s+V_{2,d}G_{pll}}\\ d & \dfrac{-bs}{s+V_{2,d}G_{pll}}\end{bmatrix}\frac{\boldsymbol{G}_{pq}I_{g,q}}{c}\tag{15}$$

where $\boldsymbol{Y}_{cl}^{pc5,m,p}$ and $\boldsymbol{Y}_{cl}^{pc5,m,q}$ are the active-current- and reactive-current-related admittance components of $\boldsymbol{Y}_{cl}^{pc5,m}$, respectively. Similar to $\boldsymbol{Y}_{ol}^{pc3,m}$ in (10), the PLL does not affect the *dd*- and *qd*-axis components of $\boldsymbol{Y}_{cl}^{pc5,m}$, while all ACC, PLL, and CLPC affect the *dq*- and *qq*-axis components. Additionally, all four components of $\boldsymbol{Y}_{cl}^{pc5,m}$ are influenced by both active and reactive currents. Specifically, active power primarily affects the *dd*- and *qq*-axis components, whereas reactive power predominantly impacts the *dq*- and *qd*-axis components. Based on (11), Fig. 8(b) establishes the equivalent circuit model of the GFLI with CLPC, where the impedance/admittance contributions of the filter, ACC, active current via PLL, reactive current via PLL, active current via CLPC, and reactive current via CLPC are modeled as $\boldsymbol{Z}_1^m$, $\boldsymbol{Z}_2^m$, $\boldsymbol{Y}_3^m$, $\boldsymbol{Y}_4^m$, $\boldsymbol{Y}_7^m$, and $\boldsymbol{Y}_8^m$, respectively. Their expressions are listed in the fifth row of Table I, and $\boldsymbol{G}_{pq}^{m2}$ is expressed as:

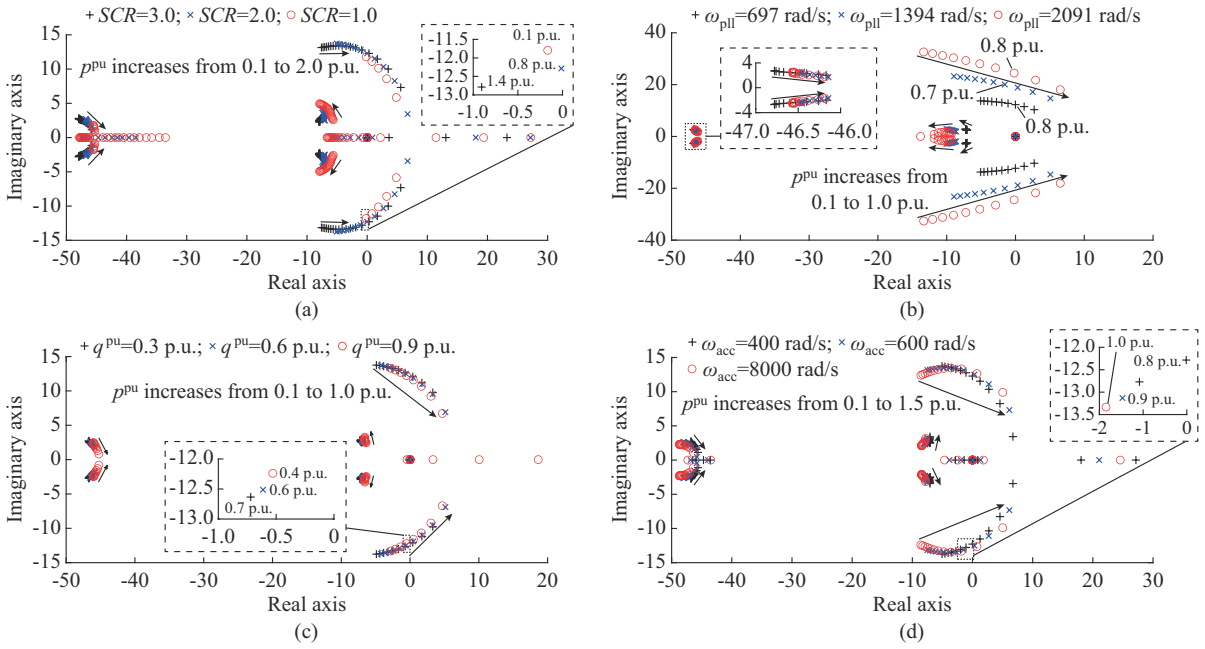

Fig. 11. Eigenvalue loci of system with OLPC as active power p^{pu} increases. (a) SCR variation with $\omega_{pll}=697$ rad/s, $q^{pu}=0$ p.u., and $\omega_{acc}=400$ rad/s. (b) PLL bandwidth ω_{pll} variation with $SCR=2.0$, $q^{pu}=0$ p.u., and $\omega_{acc}=400$ rad/s. (c) Reactive power q^{pu} variation with $SCR=2.0$, $\omega_{pll}=697$ rad/s, and $\omega_{acc}=400$ rad/s. (d) ACC bandwidth ω_{acc} variation with $SCR=2.0$, $\omega_{pll}=697$ rad/s, and $q^{pu}=0$ p.u..

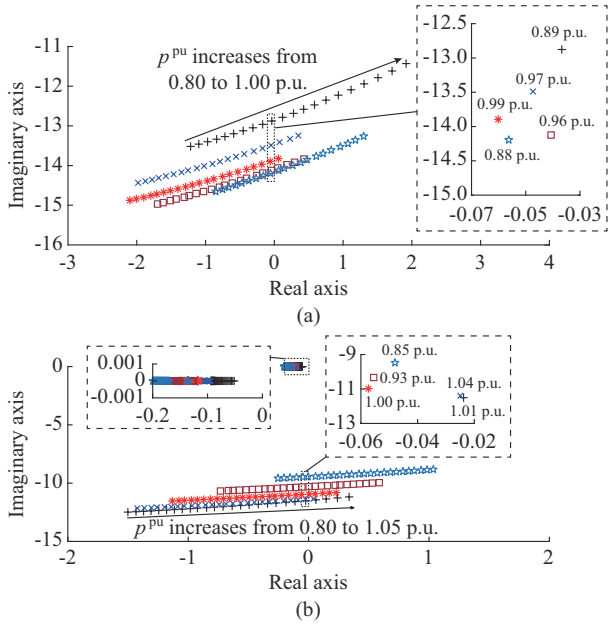

+ q^{pu}=0.3 p.u.; × q^{pu}=0.6 p.u.; * q^{pu}=0.9 p.u.; □ q^{pu}=1.2 p.u.; ☆ q^{pu}=1.5 p.u.

Fig. 12. Eigenvalue loci for $SCR=2.0$, $\omega_{pll}=697$ rad/s, $q^{pu}=0.3$, 0.6, 0.9, 1.2, 1.5 p.u., and $\omega_{acc}=400$ rad/s considering variation of PCC voltage $v^{s}_{2,d}$. (a) GFLI with OLPC. (b) GFLI with CLPC and $\omega_{pc}=40$ rad/s.

$$\boldsymbol{G}^{m2}_{pq}=\boldsymbol{I}_{2\times2}+\boldsymbol{G}^{acc,m}_{cl}\boldsymbol{G}^{m}_{pq}\boldsymbol{G}^{m}_{i,pq}\boldsymbol{G}^{m}_{i,lpf} \tag{16}$$

2) CLPC-induced MPTC

Since (10) and (15) share similar formats, the effects of active/reactive current and PLL bandwidth on the input admittance of the GFLIs with OLPC and CLPC are likely to exhibit the same trends. These trends are illustrated in Fig. 9.

Figure 14 shows the measured and analytical input admittances of the GFLI with CLPC. In the legend, the four numbers represent the values of active current $I^{pu}_{g,d}$, reactive current $I^{pu}_{g,q}$, PLL bandwidth ω_{pll}, and PC bandwidth ω_{pc}, respectively.

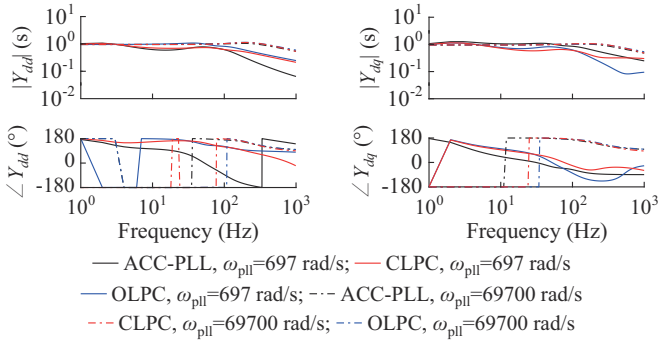

Fig. 13. Bode diagrams of *dq*- and *qq*-axis admittance components of GFLIs with ACC-PLL, OLPC, and CLPC with $p^{pu}_{ref}=1.0$ p.u., $q^{pu}_{ref}=1.0$ p.u., $\omega_{pc}=640$ rad/s, and increase of PLL bandwidth ω_{pll}.

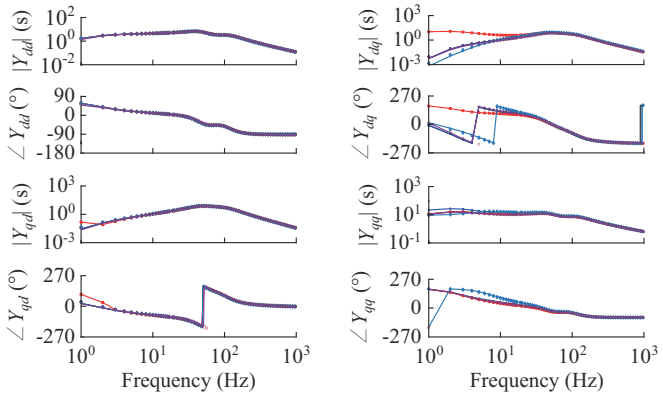

Fig. 14. Measured and analytical input admittances of GFLI with CLPC.

The grid is emulated as an ideal voltage source to maintain a constant PCC voltage $v^{s}_{2,d}$. It is clear that a large $I^{pu}_{g,d}$ primarily increases the *dd*- and *qq*-axis admittance magnitudes, whereas a large $I^{pu}_{g,q}$ mainly increases the *dq*- and *qq*-axis admittance magnitudes. The PLL affects only the *dq*- and *qq*-axis admittance components. Additionally, power controller parameters influence all four components. These observations are consistent with (15).

Figure 15 shows the eigenvalue loci of the system with CLPC. A constant PCC voltage $v^{s}_{2,d}$ is assumed to avoid violation of the power-angle relation. Compared with Figs. 4 and 11, the CLPC introduces a pair of real eigenvalues. Figure 15(a) shows that decreasing the SCR from 3.0 to 2.0 and 1.0 with $\phi = 80°$ reduces the CLPC-induced MPTC $p^{pu}_{clpc,max}$ from 1.9 p.u. to 1.1 p.u. and 0.1 p.u., respectively. The slight difference from the system with ACC and PLC, as shown in Fig. 4(a), arises because the CLPC-induced eigenvalue determines the MPTC when SCR is 3.0. Figure 15(b) indicates that increasing the PLL bandwidth ω_{pll} from 697 rad/s to 1394 rad/s and 2091 rad/s slightly decreases $p^{pu}_{clpc,max}$ from 1.1 p.u. to 1.0 p.u. and 0.9 p.u., respectively, where PLL rather than CLPC determines the MPTC. Figure 15(c) shows that increasing q^{pu} from 0.3 p.u. to 0.6 p.u. and 0.9 p.u. reduces $p^{pu}_{clpc,max}$ from 0.9 p.u. to 0.6 p.u. and 0.4 p.u., with PLL determining the MPTC in all scenarios.

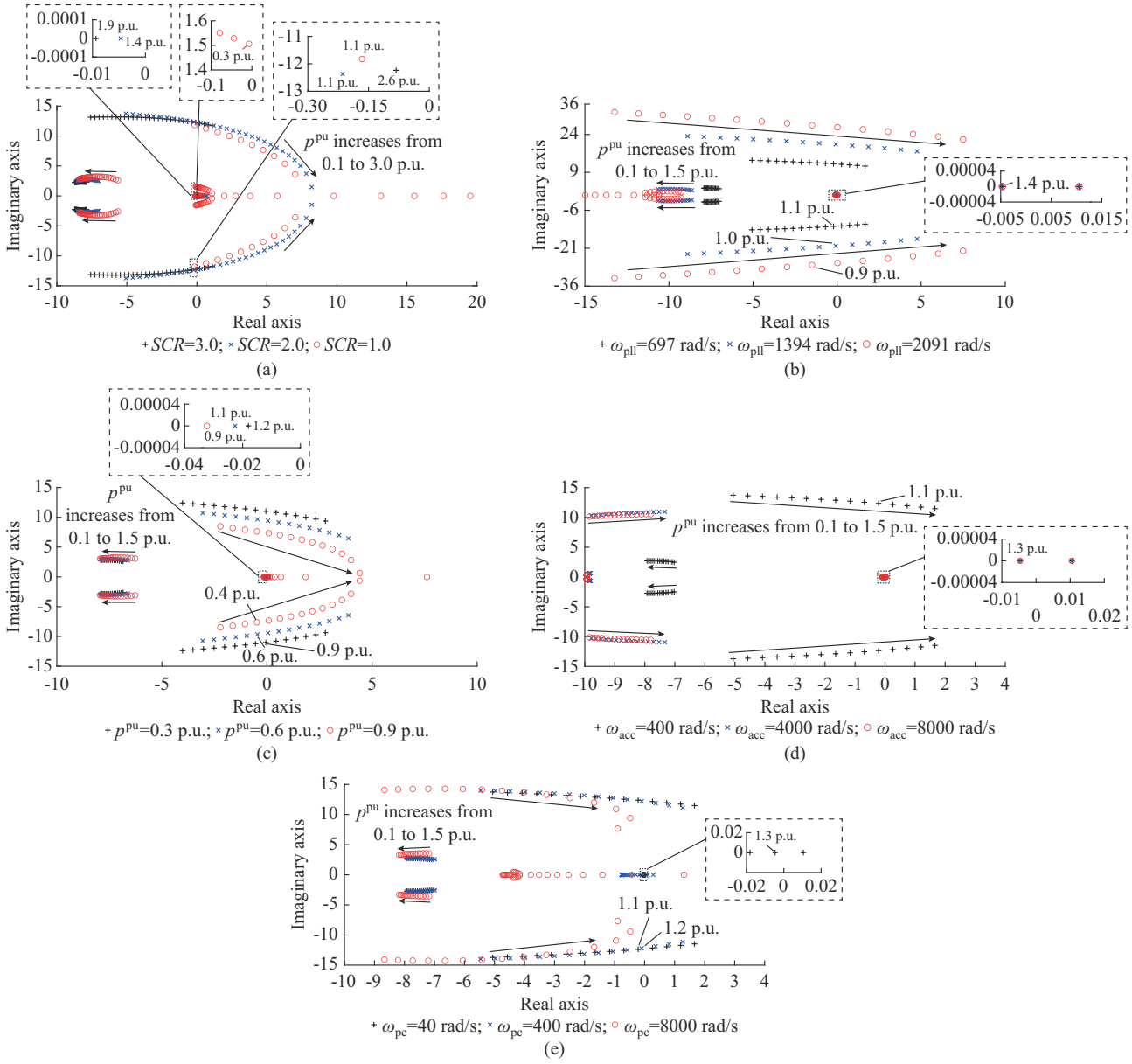

Fig. 15. Eigenvalue loci of system with CLPC as active power increases. (a) SCR variation with $\omega_{pll} = 697$ rad/s, $q^{pu} = 0$ p.u., $\omega_{acc} = 400$ rad/s, and $\omega_{pc} = 40$ rad/s. (b) PLL bandwidth variation with $SCR = 2.0$, $q^{pu} = 0$ p. u., $\omega_{acc} = 400$ rad/s, and $\omega_{pc} = 40$ rad/s. (c) Reactive power q^{pu} variation with $SCR = 2.0$, $\omega_{pll} = 1394$ rad/s, $\omega_{acc} = 400$ rad/s, and $\omega_{pc} = 40$ rad/s. (d) ACC bandwidth ω_{acc} variation with $SCR = 2.0$, $\omega_{pll} = 697$ rad/s, $q^{pu} = 0$ p.u., and $\omega_{pc} = 40$ rad/s. (e) PC bandwidth ω_{pc} variation with $SCR = 2.0$, $\omega_{pll} = 697$ rad/s, $q^{pu} = 0$ p.u., and $\omega_{acc} = 400$ rad/s.

Figure 15(d) and (e) shows that increasing both the ACC bandwidth ω_{acc} from 400 rad/s to 4000 rad/s and 8000 rad/s and the PC bandwidth ω_{pc} from 40 rad/s to 400 rad/s and 800 rad/s enhances low-frequency stability, indicating that a

fast CLPC may improve the MPTC.

Figure 12(b) shows the eigenvalue loci of the system with CLPC considering variations in the PCC voltage $v^{s}_{2,d}$. The results indicate that the MPTC $p^{pu}_{clpc,max}$ increases as q^{pu} rises from 0.3 to 0.6 p.u., but decreases as q^{pu} further increases to 1.5 p. u.. Unlike Fig. 12(a), which shows the system with OLPC, the oscillation frequency in Fig. 12(b) slightly decreases as q^{pu} increases. Additionally, the CLPC-related real eigenvalues shift to the left, stabilizing the system.

Figure 13 shows that the Bode diagrams of the *dq*- and *qq*-axis admittance components for GFLIs with ACC-PLL and CLPC converge as the PLL bandwidth ω_{pll} increases. This indicates that when the PLL is sufficiently fast, both the PLL and CLPC contribute independently to the input admittance, with no coupling between them. This observation aligns with the insight drawn for the GFLI with OLPC.

IV. Experimental Verification

Figure 16 illustrates the configuration of the scaled-down experimental setup used in the lab. The setup consists of a 320 V DC source, a line-to-line 110 V Regatron grid simulator, and a 1.896 kvar Imperix inverter controlled by a Boom-Box Imperix Controller. The rated current is 14.04 A, corresponding to a base impedance of 6.41 Ω. The SCR is set to be 1.90, with a grid impedance angle of 80°, i. e., $R_g = 585$ mΩ and $L_g = 10.56$ mH. Additionally, a 4.7 mH filter inductance and a 160 mΩ filter resistance are employed. The bandwidths of the ACC, PLL, and CLPC are 592 rad/s, 194 rad/s, and 5.92 rad/s, respectively. The PCC voltage feed-forward coefficient γ is 0.1/160. The time constants for the voltage and current low-pass filters are 20 ms and 2 ms, respectively.

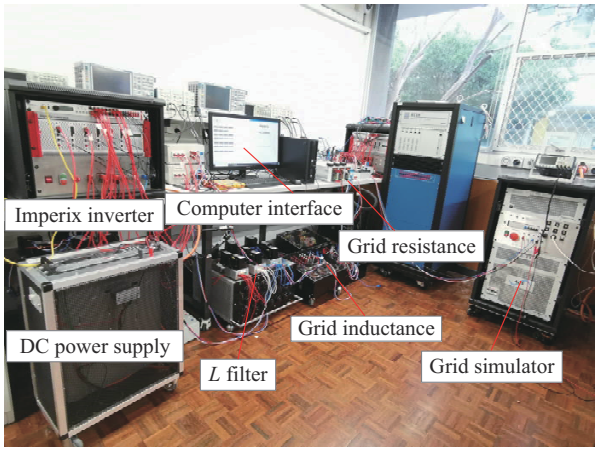

Fig. 16. Scaled-down experimental setup used in lab.

A. Verification of Effect of ACC Bandwidth on MPTC

In this experimental test, the power control is disabled. Figure 17(a)-(d) presents the experimental results of the grid current as the ACC bandwidth ω_{acc} is set to be 355.2 rad/s, 414.4 rad/s, 473.6 rad/s, and 532.8 rad/s, respectively. The results indicate that the MPTC for the four cases is 0.15 p.u., 0.3 p.u., 0.6 p.u., and 0.8 p.u., respectively, demonstrating that the MPTC increases with the ACC bandwidth.

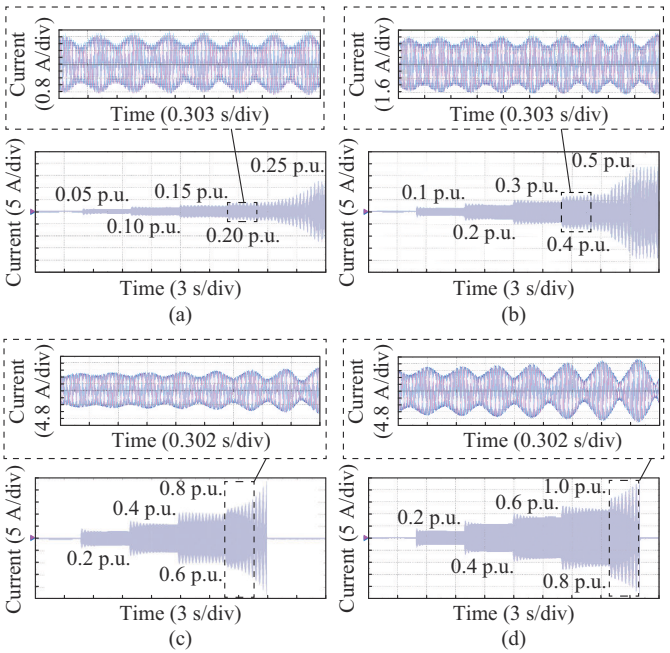

Fig. 17. Experimental results of grid current under different ACC bandwidths ω_{acc}. (a) 355.2 rad/s. (b) 414.4 rad/s. (c) 473.6 rad/s. (d) 532.8 rad/s.

B. Verification of Effect of CLPC Bandwidth on MPTC

In this experimental test, the CLPC is enabled. Figure 18(a)-(d) presents the experimental results of grid current for an ACC bandwidth of $\omega_{acc} = 355.2$ rad/s under different CLPC bandwidths ω_{pc}, which are set to be 88.8 rad/s, 118.4 rad/s, 177.6 rad/s, and 236.8 rad/s, respectively. The results show that the MPTC for the four cases is 0.15 p.u., 0.3 p.u., 0.6 p.u., and 0.8 p.u., respectively, indicating that the MPTC increases with the CLPC bandwidth.

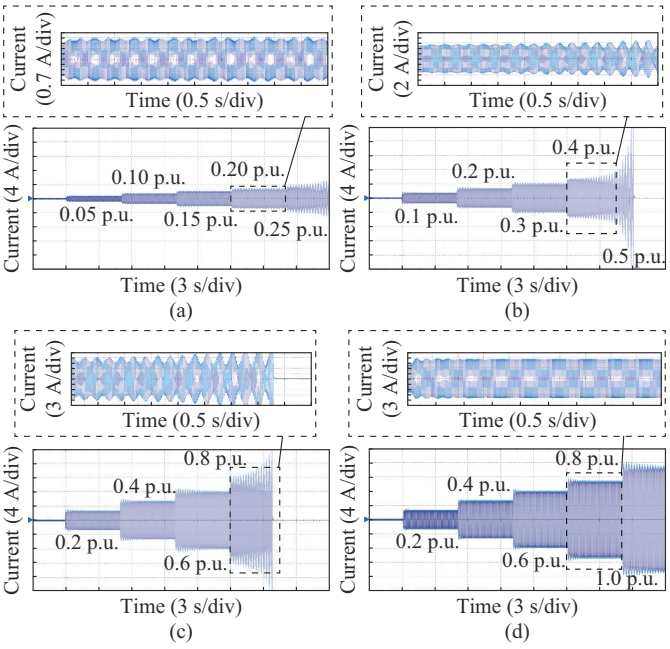

Fig. 18. Experimental results of grid current for an ACC bandwidth of $\omega_{acc} = 355.2$ rad/s under different CLPC bandwidths ω_{pc}. (a) 88.8 rad/s. (b) 118.4 rad/s. (c) 177.6 rad/s. (d) 236.8 rad/s.

Additionally, Fig. 19(a)-(d) presents the experimental results of grid current for an ACC bandwidth of $\omega_{acc}=414.4$ rad/s under different CLPC bandwidths ω_{pc}, which are set to be 5.92 rad/s, 88.8 rad/s, 106.56 rad/s, and 118.4 rad/s, respectively. The results indicate that the MPTC for these cases is 0.3 p.u., 0.4 p.u., 0.6 p.u., and 0.8 p.u., respectively. By comparing Figs. 18 and 19, it can be observed that with a faster ACC, a slower CLPC can be employed to inject the same maximum allowable active power.

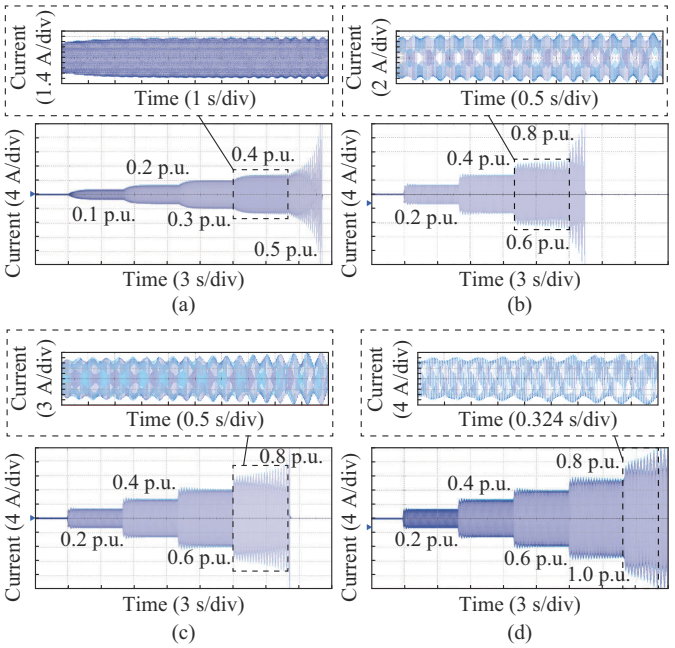

Fig. 19. Experimental results of grid current for an ACC bandwidth of $\omega_{acc}=414.4$ rad/s under different CLPC bandwidths ω_{pc}. (a) 5.92 rad/s. (b) 88.8 rad/s. (c) 106.56 rad/s. (d) 118.4 rad/s.

V. Conclusion

This paper provides a comparative investigation into the effects of control loop interactions on the static and dynamic MPTCs of PLL-based GFLIs considering various control loops. The main conclusions can be summarized as follows. Both the power-angle relation and adverse control interactions can limit the MPTC. While reactive power injection typically increases the static MPTC by providing voltage support, it can reduce the dynamic MPTC due to intensified control loop interactions. A fast ACC enhances the PLL-induced low-frequency stability but compromises high-frequency stability induced by digital time delay. The OLPC and CLPC exhibit limited admittance reshaping effects when the PLL is sufficiently fast. However, fast power control can improve the PLL-induced low-frequency stability when a slower PLL is used. Future studies could explore whether these insights can apply to other grid conditions and examine the impact of voltage control on the MPTC.

References

[1] N. Hatziargyriou, J. Milanovic, C. Rahmann *et al.*, "Definition and classification of power system stability – revisited & extended," *IEEE Transactions on Power Systems*, vol. 36, no. 4, pp. 3271-3281, Jul. 2021.

[2] *IEEE Standard for Interconnection and Interoperability of Inverter-based Resources (IBRs) Interconnecting with Associated Transmission Electric Power Systems*, IEEE Std 2800-2022, pp. 1-180, 2022.

[3] W. Zhou, N. Mohammed, and B. Bahrani, "Comprehensive modeling, analysis, and comparison of state-space and admittance models of PLL-based grid-following inverters considering different outer control modes," *IEEE Access*, vol. 10, pp. 30109-30146, Mar. 2022.

[4] Y. Cheng, L. Fan, J. Rose *et al.*, "Real-world subsynchronous oscillation events in power grids with high penetrations of inverter-based resources," *IEEE Transactions on Power Systems*, vol. 38, no. 1, pp. 316-330, Jan. 2023.

[5] N. Modi, E. M. Farahani, A. Jalali *et al.*, "Replication of real-world sub-synchronous oscillations in inverter-based resources dominated grid," *IEEE Transactions on Power Delivery*, vol. 39, no. 3, pp. 1399-1406, Jun. 2024.

[6] J. Zhou, H. Ding, S. Fan *et al.*, "Impact of short-circuit ratio and phase-locked-loop parameters on the small-signal behavior of a VSC-HVDC converter," *IEEE Transactions on Power Delivery*, vol. 29, no. 5, pp. 2287-2296, Oct. 2014.

[7] L. Huang, C. Wu, D. Zhou *et al.*, "A double-PLLs-based impedance reshaping method for extending stability range of grid-following inverter under weak grid," *IEEE Transactions on Power Electronics*, vol. 37, no. 4, pp. 4091-4104, Apr. 2022.

[8] M. Zhao, X. Yuan, J. Hu *et al.,* "Voltage dynamics of current control time-scale in a VSC-connected weak grid," *IEEE Transactions on Power Systems*, vol. 31, no. 4, pp. 2925-2937, Jul. 2016.

[9] D. Zhu, S. Zhou, X. Zou *et al.*, "Improved design of PLL controller for LCL-type grid-connected converter in weak grid," *IEEE Transactions on Power Electronics*, vol. 35, no. 5, pp. 4715-4727, May 2020.

[10] X. Li and H. Lin, "A design method of phase-locked loop for grid-connected converters considering the influence of current loops in weak grid," *IEEE Journal of Emerging and Selected Topics in Power Electronics*, vol. 8, no. 3, pp. 2420-2429, Sept. 2020.

[11] G. Wu, H. Sun, X. Zhang *et al.*, "Parameter design oriented analysis of the current control stability of the weak-grid-tied VSC," *IEEE Transactions on Power Delivery*, vol. 36, no. 3, pp. 1458-1470, Jun. 2021.

[12] S. Zhou, X. Zou, D. Zhu *et al.*, "An improved design of current controller for LCL-type grid-connected converter to reduce negative effect of PLL in weak grid," *IEEE Journal of Emerging and Selected Topics in Power Electronics*, vol. 6, no. 2, pp. 648-663, Jun. 2018.

[13] H. Gong, X. Wang, and L. Harnefors, "Rethinking current controller design for PLL-synchronized VSCs in weak grids," *IEEE Transactions on Power Electronics*, vol. 37, no. 2, pp. 1369-1381, Feb. 2022.

[14] S. Silwal, M. Karimi-Ghartemani, H. Karimi *et al.*, "A multivariable controller in synchronous frame integrating phase-locked loop to enhance performance of three-phase grid-connected inverters in weak grids," *IEEE Transactions on Power Electronics*, vol. 37, no. 9, pp. 10 348-10 359, Sept. 2022.

[15] Z. Xie, Y. Chen, W. Wu *et al.*, "Stability enhancing voltage feed-forward inverter control method to reduce the effects of phase-locked loop and grid impedance," *IEEE Journal of Emerging and Selected Topics in Power Electronics*, vol. 9, no. 3, pp. 3000-3009, Jun. 2021.

[16] W. Zhou, N. Mohammed, and B. Bahrani, "Voltage and current dynamics cancellation of weak-grid-tied grid-following inverters for maximum transferable power improvement," *IEEE Transactions on Energy Conversion*, vol. 39, no. 3, pp. 2053-2067, Sept. 2024.

[17] Y. Li, L. Fan, and Z. Miao, "Stability control for wind in weak grids," *IEEE Transactions on Sustainable Energy*, vol. 10, no. 4, pp. 2094-2103, Oct. 2019.

[18] L. Fan, "Modeling type-4 wind in weak grids," *IEEE Transactions on Sustainable Energy*, vol. 10, no. 2, pp. 853-864, Apr. 2019.

[19] G. Wu, J. Liang, X. Zhou *et al.*, "Analysis and design of vector control for VSC-HVDC connected to weak grids," *CSEE Journal of Power and Energy Systems*, vol. 3, no. 2, pp. 115-124, Jun. 2017.

[20] C. Collados-Rodriguez, M. Cheah-Mane, E. Prieto-Araujo *et al.*, "Stability analysis of systems with high VSC penetration: where is the limit?" *IEEE Transactions on Power Delivery*, vol. 35, no. 4, pp. 2021-2031, Aug. 2020.

[21] C. Li, S. Wang, and J. Liang, "Tuning method of a grid-following converter for the extremely-weak-grid connection," *IEEE Transactions on Power Systems*, vol. 37, no. 4, pp. 3169-3172, Jul. 2022.

[22] Y. Huang and D. Wang, "Effect of control-loops interactions on power stability limits of VSC integrated to AC system," *IEEE Transactions on Power Delivery*, vol. 33, no. 1, pp. 301-310, Feb. 2018.

[23] A. J. Agbemuko, J. L. Domìnguez-Garcìa, O. Gomis-Bellmunt *et al.*, "Passivity-based analysis and enhancement of a vector controlled VSC

connected to a weak AC grid," *IEEE Transactions on Power Delivery*, vol. 36, no. 1, pp. 156-167, Feb. 2021.
[24] D. Wang, L. Liang, L. Shi *et al.*, "Analysis of modal resonance between PLL and DC-link voltage control in weak-grid tied VSCs," *IEEE Transactions on Power Systems*, vol. 34, no. 2, pp. 1127-1138, Mar. 2019.
[25] Y. Huang, X. Yuan, J. Hu *et al.*, "DC-bus voltage control stability affected by AC-bus voltage control in VSCs connected to weak AC grids," *IEEE Journal of Emerging and Selected Topics in Power Electronics*, vol. 4, no. 2, pp. 445-458, Jun. 2016.
[26] J. Hu, Y. Huang, D. Wang *et al.*, "Modeling of grid-connected DFIG-based wind turbines for DC-link voltage stability analysis," *IEEE Transactions on Sustainable Energy*, vol. 6, no. 4, pp. 1325-1336, Oct. 2015.
[27] W. Zhou, Y. Wang, R. E. Torres-Olguin *et al.*, "Effect of reactive power characteristic of offshore wind power plant on low-frequency stability," *IEEE Transactions on Energy Conversion*, vol. 35, no. 2, pp. 837-853, Jun. 2020.
[28] W. Zhou, Y. Wang. R. E. Torres-Olguin, "*DQ* impedance reshaping of three-phase power-controlled grid-connected inverter for low-frequency stability improvement under weak grid condition," in *Proceedings of IEEE Energy Conversion Congress and Exposition (ECCE)*, Detroit, USA, Oct. 2020, pp. 1678-1685.
[29] G. Wu, H. Sun, B. Zhao *et al.*, "Low-frequency converter-driven oscillations in weak grids: explanation and damping improvement," *IEEE Transactions Power Systems*, vol. 36, no. 6, pp. 5944-5947, Nov. 2021.
[30] J. F. Morris, K. H. Ahmed, and A. Egea-Alvarez, "Analysis of controller bandwidth interactions for vector-controlled VSC connected to very weak AC grids," *IEEE Journal of Emerging and Selected Topics in Power Electronics*, vol. 9, no. 6, pp. 7343-7354, Dec. 2021.
[31] C. Henderson, A. Egea-Alvarez, S. Fekriasl *et al.*, "The effect of grid-connected converter control topology on the diagonal dominance of converter output impedance," *IEEE Open Access Journal of Power and Energy*, vol. 10, pp. 617-628, Sept. 2023.

Weihua Zhou received the B.Eng. and M.Sc. degrees in electrical engineering from Northwestern Polytechnical University, Xi'an, China, in 2014 and 2017, respectively. He received the Ph.D. degree in power electronics from Aalborg University, Aalborg, Denmark, in 2020. He was a Research Fellow at Monash University, Melbourne, Australia. He is currently with the Australian Energy Market Operator, Melbourne, Australia. His research interests include modeling, analysis, and control of inverter-based resources.

Mohammad Hasan Ravanji received the B.Sc., M.Sc., and Ph.D. degrees from Sharif University of Technology, Tehran, Iran, in 2012, 2014, and 2020, respectively, all in electrical engineering. He was a Visiting Student at the University of Waterloo, Waterloo, Canada, from October 2017 to April 2018. He is currently an Assistant Professor with the Department of Electrical Engineering at Sharif University of Technology (SUT), Tehran, Iran. His research interests include design, control, analysis, dynamics, and operation of inverter-based resources.

Nabil Mohammed received the bachelor's degree (Hons.) in electrical power engineering from Tishreen University, Latakia, Syria, in 2013, the M.Eng. degree in electrical engineering from Universiti Teknologi Malaysia, Johor Bahru, Malaysia, in 2017, and the Ph.D. degree in power electronics from Macquarie University, Sydney, Australia, in 2022. He is currently a Postdoctoral Research Fellow with Monash University, Melbourne, Australia. His research interests include modeling and control of electric systems.

Behrooz Bahrani received the B.Sc. degree from Sharif University of Technology, Tehran, Iran, the M.Sc. degree from the University of Toronto, Toronto, Canada, and the Ph.D. degree from Ecole Polytechnique Fédérale de Lausanne (EPFL), Lausanne, Switzerland, in 2006, 2008, and 2012, respectively, all in electrical engineering. He is currently an Associate Professor at Monash University, Melbourne, Australia. His research interests include control of power electronic systems, application of power electronics in power and traction systems, and grid integration of renewable energy resources.